0026-895X/11/8005-796–808$25.00
MOLECULAR PHARMACOLOGY
Vol. 80, No. 5
72207/3723735
*Mol Pharmacol* 80:796–808, 2011
*Printed in U.S.A.*




# A Dynamic Pharmacophore Drives the Interaction between Psalmotoxin-1 and the Putative Drug Target Acid-Sensing Ion Channel 1a[S]

Natalie J. Saez, Mehdi Mobli, Michael Bieri, Irène R. Chassagnon, Alpeshkumar K. Malde, Roland Gamsjaeger, Alan E. Mark, Paul R. Gooley, Lachlan D. Rash, and Glenn F. King

*Institute for Molecular Bioscience (N.J.S., M.M., I.R.C., A.E.M., L.D.R., G.F.K.) and School of Chemistry and Molecular Biosciences (A.K.M., A.E.M.), The University of Queensland, St. Lucia, Queensland, Australia; Department of Biochemistry & Molecular Biology, Bio21 Molecular Science & Biotechnology Institute, University of Melbourne, Parkville, Victoria, Australia (M.B., P.R.G.); and School of Molecular and Microbial Biosciences, the University of Sydney, Sydney, New South Wales, Australia (R.G.)*

Received March 12, 2011; accepted August 8, 2011

## ABSTRACT

Acid-sensing ion channel 1a (ASIC1a) is a primary acid sensor in the peripheral and central nervous system. It has been implicated as a novel therapeutic target for a broad range of pathophysiological conditions including pain, ischemic stroke, depression, and autoimmune diseases such as multiple sclerosis. The only known selective blocker of ASIC1a is $\pi$-TRTX-Pc1a (PcTx1), a disulfide-rich 40-residue peptide isolated from spider venom. $\pi$-TRTX-Pc1a is an effective analgesic in rodent models of acute pain and it provides neuroprotection in a mouse model of ischemic stroke. Thus, understanding the molecular basis of the $\pi$-TRTX-Pc1a–ASIC1a interaction should facilitate development of therapeutically useful ASIC1a blockers. We therefore developed an efficient bacterial expression system to produce a panel of $\pi$-TRTX-Pc1a mutants for probing structure-activity relationships as well as isotopically labeled toxin for determination of its solution structure and dynamics. We demonstrate that the toxin pharmacophore resides in a $\beta$-hairpin loop that was revealed to be mobile over a wide range of time scales using molecular dynamics simulations in combination with NMR spin relaxation and relaxation dispersion measurements. The toxin-receptor interaction was modeled by in silico docking of the toxin structure onto a homology model of rat ASIC1a in a restraints-driven approach that was designed to take account of the dynamics of the toxin pharmacophore and the consequent remodeling of side-chain conformations upon receptor binding. The resulting model reveals new insights into the mechanism of action of $\pi$-TRTX-Pc1a and provides an experimentally validated template for the rational design of therapeutically useful $\pi$-TRTX-Pc1a mimetics.

## Introduction

It was recognized over 25 years ago that small-diameter trigeminal neurons depolarize in response to mild decreases in pH (Krishtal and Pidoplichko, 1981). However, acid-sensing ion channels (ASICs) were not discovered and recognized as neuronal proton sensors until 1997 (Waldmann et al., 1997). ASICs are now thought to be a primary sensor of pain associated with local tissue acidosis resulting from (patho) physiological conditions such as inflammation, ischemia, infection, physical trauma, and tumors (Sluka et al., 2009).

This work was supported by the National Health and Medical Research Council of Australia [Project Grant 511067]; and the Australian Research Council [Discovery Grants DP0878608, DP0987043, DP0879065]. N.J.S. was supported by an Australian Postgraduate Award from the Australian Research Council. M.B. was supported by postdoctoral fellowships from the Swiss National Science Foundation [Fellowships PBBEP3-125613, PA00P3-134167].

Article, publication date, and citation information can be found at http://molpharm.aspetjournals.org.

doi:10.1124/mol.111.072207.

[S] The online version of this article (available at http://molpharm.aspetjournals.org) contains supplemental material.

**ABBREVIATIONS:** ASIC, acid-sensing ion channel; PcTx1, *Psalmopoeus cambridgei* toxin-1 (psalmotoxin-1); $\pi$-TRTX-Pc1a, $\pi$-theraphotoxin-Pc1a; MBP, maltose binding protein; TEV, tobacco etch virus; IPTG, isopropyl $\beta$-D-1-thiogalactopyranoside; Ni-NTA, nickel-nitrilotriacetic acid; HPLC, high-performance liquid chromatography; rpHPLC, reversed-phase high-performance liquid chromatography; MALDI-TOF, matrix-assisted laser desorption ionization/time of flight; MS, mass spectroscopy; NUS, nonuniform sampling; HSQC, heteronuclear single quantum correlation; NOESY, nuclear Overhauser effect (or enhancement) spectroscopy; HNHB, (amide proton)-(nitrogen)-($\beta$-proton) correlation; NOE, nuclear Overhauser effect; 3D, three dimensional; CPMG, Carr-Purcell-Meiboom-Gill; MD, molecular dynamics; ECD, extracellular domain; TM, transmembrane; PDB, Protein Data Bank; AIR, ambiguous interaction restraint; $R_1$, longitudinal relaxation rate; $R_2$, transverse relaxation rate; $R_{ex}$, chemical/conformational exchange rate constant.

ASICs belong to the epithelial sodium channel/degenerin (ENaC/DEG) superfamily of ion channels, which have the same overall topology and selectivity for transporting sodium (Kellenberger and Schild, 2002). However, ASICs are distinguished by their restriction to chordates, their predominantly neuronal distribution, and their activation by a decrease in extracellular pH (Gründer and Chen, 2010). There are four ASIC subtypes (ASIC1, ASIC2, ASIC3, and ASIC4), encoded by four distinct genes, two of these having alternatively spliced forms (ASIC1a/ASIC1b and ASIC2a/ASIC2b). Functional ASIC channels consist of homo- or heterotrimeric assemblies of these subunits (Jasti et al., 2007; Carnally et al., 2008), each with unique pH sensitivities and kinetics (Hesselager et al., 2004).

ASIC1a is the most abundant ASIC subunit in the central nervous system and, along with ASIC3, has the highest affinity for protons (Gründer and Chen, 2010). Homomeric ASIC1a channels activate at pH 6.9, and the current amplitude increases as the proton concentration increases down to pH 6.0 (Gründer and Chen, 2010). Various studies support a role for ASIC1a in mediating both inflammatory and neuropathic pain, and an undisclosed compound that is purported to be a selective antagonist of ASIC1a reduces thermal and mechanical hyperalgesia in a human inflammatory pain model (Dubé et al., 2009). In addition, ASIC1a seems to play an important role in fear conditioning, epileptic seizure termination, autoimmune disease, and ischemia-induced neurodegeneration (Xiong et al., 2008; Dubé et al., 2009; Sluka et al., 2009; Gründer and Chen, 2010). Thus, ASIC1a has been touted as a novel therapeutic target for a broad range of pathophysiological conditions, including pain, ischemic stroke, depression, and autoimmune diseases (Xiong et al., 2008; Dubé et al., 2009; Sluka et al., 2009; Gründer and Chen, 2010).

Several small molecule ASIC1a blockers have been reported, but they are mostly weak and nonselective. The diuretic drug amiloride blocks all ASIC subtypes with moderate potency ($IC_{50}$, ~10–50 μM), whereas several nonsteroidal anti-inflammatory drugs such as ibuprofen weakly inhibit ASIC1a ($IC_{50}$, ~350 μM) (Xiong et al., 2008). Antiprotozoal diarylamidines also nonselectively block ASICs with low micromolar potency (Chen et al., 2010). The most potent and selective blocker of ASIC1a is psalmotoxin-1 (PcTx1), a 40-residue peptide isolated from the venom of the tarantula *Psalmopoeus cambridgei*. PcTx1 [hereafter called π-theraphotoxin-Pc1a (π-TRTX-Pc1a) based on the rational nomenclature for naming peptide toxins (King et al., 2008)] inhibits ASIC1a channels with an $IC_{50}$ of ~1 nM, but does not block other ASIC subtypes at concentrations up to 50 nM (Escoubas et al., 2000). At higher concentrations ($EC_{50}$, ~100–140 nM) π-TRTX-Pc1a also positively modulates rat ASIC1b (Chen et al., 2006). π-TRTX-Pc1a is an effective analgesic, comparable with morphine, in rodent models of acute pain (Mazzuca et al., 2007) and intranasal administration of π-TRTX-Pc1a provided neuroprotection in a mouse model of ischemic stroke, even when administered hours after injury (Pignataro et al., 2007).

A low-resolution solution structure of π-TRTX-Pc1a was determined previously, and the channel interaction surface was proposed to reside in a highly cationic β-hairpin loop (Escoubas et al., 2003). In two recent studies (Pietra, 2009; Qadri et al., 2009), this structure of π-TRTX-Pc1a was docked onto a homology model of human ASIC1a and, in both cases, the toxin was found to interact with the acidic pocket on the channel ectodomain that plays a critical role in proton binding. However, the toxin orientation differs between the two models, and the precise molecular details of the toxin-channel interaction remain uncertain.

To provide a better understanding of the mechanism of action of π-TRTX-Pc1a, we developed a bacterial expression system for producing π-TRTX-Pc1a mutants for functional analysis and isotopically labeled protein for determination of a high quality structure. Mutagenesis studies, in combination with NMR relaxation data and molecular dynamics simulations, revealed that the key pharmacophore residues are located in a β-hairpin loop that undergoes significant motion in solution. Experimental restraints were used to dock our new high-resolution structure of π-TRTX-Pc1a onto ASIC1a. The resulting model of the π-TRTX-Pc1a–ASIC1a complex differs substantially from previously published models, and it offers new insights into the mechanism by which π-TRTX-Pc1a modulates the activity of ASIC1a.

## Materials and Methods

**Production of Recombinant π-TRTX-Pc1a.** A synthetic gene encoding π-TRTX-Pc1a, or point mutants thereof, with codons optimized for expression in *Escherichia coli*, was cloned into a variant of the pLic-MBP expression vector expression (Cabrita et al., 2006). This vector encodes a MalE signal sequence for periplasmic export, a $His_6$ affinity tag, a maltose binding protein (MBP) fusion tag (to aid solubility), and a tobacco etch virus (TEV) protease recognition site directly preceding the π-TRTX-Pc1a gene (Fig. 1A). Plasmids were transformed into *E. coli* strain BL21(λDE3) for recombinant toxin production.

Cultures were grown in Luria-Bertani medium at 37°C with shaking at 180 rpm. Expression of the toxin gene was induced with 1 mM IPTG at an $OD_{600}$ of 1.0 to 1.2 and cells were harvested 3 h later by centrifugation for 10 min at 7741 *g*. For production of uniformly $^{13}C/^{15}N$-labeled π-TRTX-Pc1a, cultures were grown in minimal medium supplemented with $^{13}C_6$-glucose and $^{15}NH_4Cl$ as the sole carbon and nitrogen sources, respectively.

The $His_6$-MBP-toxin fusion protein was extracted from the bacterial periplasm by osmotic shock using 30 mM Tris, 40% sucrose, 2 mM EDTA pH 8.0, and ice-cold water. The $His_6$-MBP-toxin fusion protein was captured by passing the periplasmic extract (buffered in 20 mM Tris, 200 mM NaCl, 10% glycerol, pH 8.0) over Ni-NTA Superflow resin (QIAGEN, Valencia, CA) followed by washing with 15 mM imidazole to remove nonspecific binders. The fusion protein was then eluted with 250 mM imidazole. The buffer was exchanged to remove imidazole, then reduced and oxidized glutathione were added to 3 and 0.3 mM, respectively, to activate TEV protease and promote folding of the protein. Approximately 40 μg of $His_6$-tagged TEV protease was added per mg of π-TRTX-Pc1a, and the cleavage reaction was allowed to proceed at room temperature for 12 h. The cleaved $His_6$-MBP and $His_6$-TEV were removed by passing the solution over Ni-NTA Superflow resin, whereas the eluate containing cleaved π-TRTX-Pc1a was collected for further purification using reversed-phase (rp) HPLC. rpHPLC was performed on a Vydac $C_{18}$ column (250 × 4.6 mm; particle size, 5 μm) using a flow rate of 1 ml/min and a gradient of 20 to 40% solvent B (0.1% trifluoroacetic acid in 90% acetonitrile) in solvent A (0.1% trifluoroacetic acid in water) over 40 min. To facilitate comparisons with other studies on π-TRTX-Pc1a, residue numbers for the native toxin are used throughout the text even though the recombinant toxin contains an additional N-terminal serine residue that is a vestige of the TEV cleavage site.

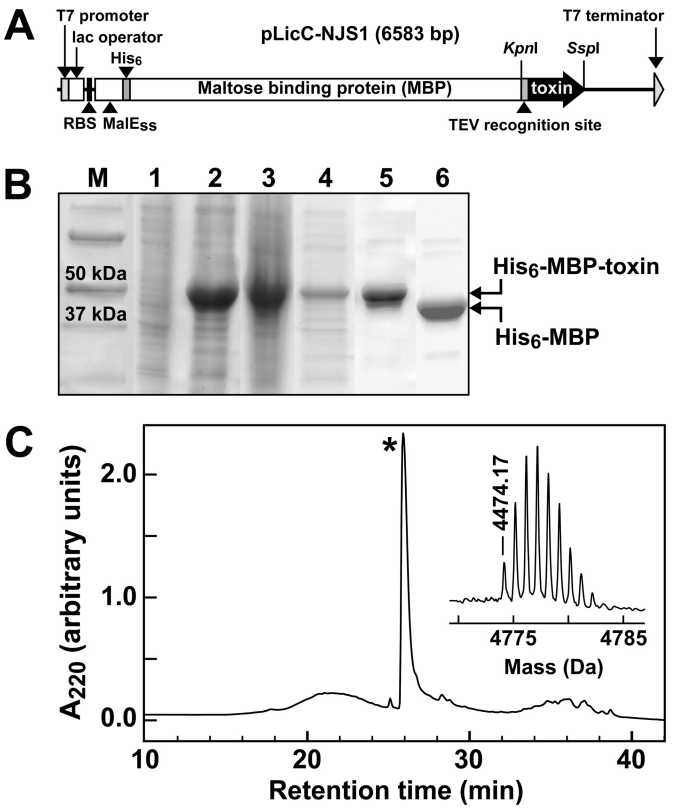


**Fig. 1.** Expression and purification of recombinant $\pi$-TRTX-Pc1a. A, schematic of the pLicC-NJS1 vector used for periplasmic expression of $\pi$-TRTX-Pc1a. The coding region includes a MalE signal sequence ($MalE_{SS}$) for periplasmic export, a $His_6$ affinity tag, an MBP fusion tag, and a codon-optimized gene encoding $\pi$-TRTX-Pc1a, with a TEV protease recognition site inserted between the MBP and toxin coding regions. The locations of key elements of the vector are shown, including the ribosome binding site (RBS). B, SDS-polyacrylamide gel illustrating various steps in the purification of $\pi$-TRTX-Pc1a. Lanes are as follows: M, molecular mass markers; 1, cell extract before IPTG induction; 2, extract from IPTG-induced cells; 3, extract from osmotic shock treatment (sucrose-enriched cells in water); 4, soluble periplasmic extract; 5, fusion protein eluted from Ni-NTA column before TEV cleavage; 6, postcleavage sample. C, rpHPLC chromatogram showing the final step in the purification of $\pi$-TRTX-Pc1a; the asterisk denotes the peak corresponding to correctly folded recombinant toxin. The inset is a MALDI-TOF MS spectrum showing the $M+H^+$ ion for the purified recombinant toxin (observed, 4774.17 Da; calculated, 4774.21 Da).

**MALDI-TOF Mass Spectrometry.** Toxin masses were confirmed by matrix-assisted laser desorption ionization–time-of-flight mass spectrometry (MALDI-TOF MS) using a model 4700 Proteomics Bioanalyser (Applied Biosystems, Foster City, CA). rpHPLC fractions were mixed [1:1 (v/v)] with $\alpha$-cyano-4-hydroxy-cinnamic acid matrix (5 mg/ml in 50/50 acetonitrile/$H_2O$) and MALDI-TOF spectra were collected in positive reflector mode. All masses given are for the monoisotopic $M+H^+$ ions.

**Electrophysiological Measurements.** Toxin activity was assessed using two-electrode voltage-clamp experiments performed on *Xenopus laevis* oocytes expressing homomeric rat ASIC channels. Oocyte preparation, cRNA injection, and electrophysiology were performed as described previously (Jensen et al., 2009). In brief, oocytes were injected with rat ASIC1a (0.25 ng), ASIC1b (1 ng), ASIC2a (2 ng), or ASIC3 (2.5 ng) cRNA, and experiments were performed at room temperature (21–22°C) 2 to 5 days after cRNA injection. Oocytes were clamped at −60 mV (OC-725C oocyte clamp; Warner Instruments, Hamden, CT) using two standard glass microelectrodes (0.5–2 MΩ) filled with 3 M KCl solution. Data acquisition and analysis were performed using pCLAMP software, version 8 (Molecular Devices, Sunnyvale, CA). Currents were elicited by a drop in pH from 7.45 to 6.0 every 60 s using a microperfusion system to allow rapid solution exchange. Serial dilutions of $\pi$-TRTX-Pc1a (from 10 pM to 30 nM) were administered after stimulation at pH 7.45, and oocytes were bathed in the toxin solution until the next round of stimulation. The effect of native and mutant $\pi$-TRTX-Pc1a on steady-state desensitization of rASIC1a was determined by applying twice the determined $IC_{50}$ for each peptide at various conditioning pH values from 7.60 to 7.00 for 120 s before stimulation by a pH drop to 6.0. All experiments were performed using ND96 solution spiked with 0.1% bovine serum albumin to minimize adsorption of $\pi$-TRTX-Pc1a to plastic tubing. Statistics were performed using Prism 5.0c for Mac OS X (GraphPad Software, San Diego, CA).

**Structure Determination.** Lyophilized recombinant $\pi$-TRTX-Pc1a was resuspended at a final concentration of 300 $\mu$M in 10 mM sodium phosphate buffer, pH 6.0, constituted in either 92.5% $H_2O$/7.5% $D_2O$ or 100% $D_2O$. The sample was filtered using a low-protein-binding Ultrafree-MC centrifugal filter (0.22-um pore size; Millipore, Billerica, MA), then 300 $\mu$l was added to a susceptibility-matched 5-mm outer diameter microtube (Shigemi Inc., Japan).

Data were acquired at 298 K using a 900 MHz NMR spectrometer (Bruker BioSpin GmbH, Rheinstetten, Germany) equipped with a cryogenically cooled probe. Data for resonance assignments were acquired using nonuniform sampling (NUS). Sampling schedules that approximated the signal decay in each indirect dimension were generated using sched3D (Mobli et al., 2010). Pulse programs were modified from the standard Bruker library for NUS mode and are available from the authors upon request. NUS data were processed using the Rowland NMR toolkit (http://www.rowland.org/rnmrtk/toolkit.html) and maximum entropy parameters were automatically selected as described previously (Mobli et al., 2007).

$^{13}C$- and $^{15}N$-edited HSQC-NOESY (mixing time of 250 ms), (amide proton)-(nitrogen)-($\beta$-proton) correlation (HNHB), and long-range HNCO experiments were acquired using uniform sampling. All experiments were acquired in $H_2O$ except for the $^{13}C$-edited HSQC-NOESY, which was acquired in $D_2O$.

Dihedral-angles (20 $\phi$, 22 $\psi$) were derived from TALOS chemical shift analysis (Cornilescu et al., 1999), and the restraint range for structure calculations was set to twice the estimated S.D. Eight additional $\phi$ restraints of $-105 \pm 75°$ were applied for residues for which the intraresidue $H_\alpha$-$H_N$ NOE was clearly weaker than that between the $H_N$ and $H_\alpha$ of the preceding residue (Fletcher et al., 1997). All three X-Pro peptide bonds were identified as *trans* on the basis of characteristic NOEs and the $C_\alpha$ and $C_\beta$ chemical shifts of the Pro residues. The magnitude of the $^3J_{HNH\beta}$ couplings measured qualitatively from a 3D HNHB spectrum were used in combination with $H_\alpha$-$H_\beta$ and $H_N$-$H_\beta$ NOESY cross-peak intensities to obtain $\chi_1$ restraints and stereospecific assignments for 11 pairs of $\beta$-methylene protons as well as $\chi_1$ restraints for Ile4 and Val34. Additional stereospecific assignments were obtained from preliminary structure calculations, including the methyl groups of all Val and Leu residues.

Hydrogen bonds were identified by acquiring a long-range HNCO experiment and by using preliminary structures to identify the hydrogen-bond acceptor for slowly exchanging amide protons identified by their presence in the $^{13}C$-edited NOESY-HSQC spectrum acquired days after reconstitution of the lyophilized protein in $D_2O$. Hydrogen- and disulfide-bond restraints were applied as described previously (Fletcher et al., 1997).

NOESY spectra were manually peak picked and integrated, then peaklists were automatically assigned, distance restraints extracted, and an ensemble of structures calculated using the torsion angle dynamics package CYANA (Güntert, 2004). The tolerances used for CYANA were 0.03 ppm in the direct $^1H$ dimension, 0.035 ppm in the indirect $^1H$ dimension, and 0.25 ppm for the heteronucleus ($^{13}C/^{15}N$). During the automated NOESY assignment/structure calculation process, CYANA assigned 89% of all NOESY cross-peaks (1391 of 1566).

**Spin Relaxation Data Analysis.** NMR experiments for measuring $\{^1H\}$-$^{15}N$ steady-state NOE and longitudinal ($R_1$) and transverse

($R_2$) $^{15}$N relaxation rates were acquired using single-scan interleaved pulse sequences on 600- and 800-MHz Bruker spectrometers equipped with *z*-gradient cryoprobes. Data were acquired at 298 K using a 450 μM sample of $^{13}$C/$^{15}$N labeled π-TRTX-Pc1a. A $^{13}$C refocussing pulse was used during $^{15}$N evolution, and a heat compensation cycle was placed in the recovery time of $R_2$ experiments. $R_1$ spectra were recorded with eight delay times (2 × 0.01, 0.05, 0.1, 2 × 0.3, 0.5, 0.7, 2 × 0.9, and 1.1 s) at both 600 and 800 MHz; $R_2$ spectra were recorded with seven delay times (600 MHz, 2 × 0.016064, 0.032128, 0.064256, 2 × 0.096384, 0.128512, 2 × 0.16064, 0.192768 s; 800 MHz, 2 × 0.0144256, 0.0288512, 0.0577024, 2 × 0.0865536, 0.1154048, 2 × 0.144256, 0.1731072 s). {$^1$H}-$^{15}$N NOE spectra were acquired with a saturation delay of 4 s and an additional 5 s of relaxation. Spectra were processed using NMRPipe (http://spin.niddk.nih.gov/NMRPipe/) and analyzed using Sparky (http://www.cgl.ucsf.edu/home/sparky/). Model-free analysis was performed using relaxGUI (Bieri et al, 2011).

**$R_2$ Relaxation Dispersion Data Analysis.** $^{15}$N $R_2$ relaxation rates were measured at 298 K using single-scan interleaved constant time CPMG pulse sequences with a delay of 0.08 s ($T_{CPMG}$) on a Bruker 600 MHz spectrometer. Relaxation dispersion profiles were produced by recording spectra with varying CPMG field strengths (25, 2 × 50, 75, 100, 2 × 150, 2 × 200, 300, 500, 600, 700, 900, 1000, 1500, and 2000 Hz). A reference spectrum without a CPMG pulse train was also recorded. Data fitting, model selection, and simulation were performed using the software NESSY (http://home.gna.org/nessy/).

**Molecular Dynamics Simulations of π-TRTX-Pc1a.** MD simulations of π-TRTX-Pc1a in explicit water (SPC model) were performed using GROMACS version 3.3.1 (Van Der Spoel et al., 2005) in conjunction with the GROMOS 53a6 force field (Oostenbrink et al., 2004). The starting structure for simulations was the first model from the ensemble of π-TRTX-Pc1a structures determined in the current study. The protonation states of ionizable side chains were set to pH 6.0, the pH at which the structure was determined and at which ASIC1a is activated under physiological conditions. The His14 residue in π-TRTX-Pc1a could be positively charged or neutral at pH 6.0; therefore, two systems were simulated. In system 1, both the Nδ and Nε of His14 were protonated (His14 positively charged). In system 2, only the Nε was protonated (His14 neutral). As the experimental NMR studies were performed at low salt concentration, systems 1 and 2 were simulated in the absence of counter-ions. Each system was simulated twice for 5 ns (four simulations in total) using an integration time-step of 2 fs. Further details of the Monte Carlo simulation parameters are provided in Supplemental Data. Order parameters were calculated from the simulations using the equation

$$S^2 = \frac{1}{2}\left[3\sum_{\alpha=1}^{3}\sum_{\beta=1}^{3}\langle\mu_\alpha\mu_\beta\rangle^2 - 1\right]$$

where $\mu_\alpha$ ($\alpha$ = 1, 2, 3) are the *x*, *y*, and *z* components of the normalized interatomic vector in the molecular frame. In the experiment, the timeframe probed by $S^2$ is dependent on the rotational correlation time of the molecule. Given that the length of the trajectories is insufficient to average over the rotational degrees of freedom, the correlation functions and order parameters were calculated after a least-squares fit on the backbone atoms (i.e., $C_\alpha$, C′, and N). To correct for bias introduced using this approach, the trajectory was analyzed by averaging the values over 100-, 200-, and 500-ps windows.

**Construction of a Homology Model of Rat ASIC1a.** Homology modeling was performed using Modeler 9 ver. 2 (Eswar et al., 2006). The 1.9-Å resolution crystal structure of chicken ASIC1 (cASIC1) (PDB code 2QTS; Jasti et al., 2007) was used as a template for the extracellular domain (ECD) of rat ASIC1a (rASIC1a), whereas the 3-Å resolution structure of a more complete cASIC1 construct (PDB code 3HGC; Gonzales et al., 2009) was used as the template for the transmembrane (TM) regions. Truncations were made to the N and C termini based on the residues missing from the crystal structures (chain A, Δ1–40 and 458–526; chain B, Δ1–40 and 461–526; chain C, Δ1–38 and 457–526). An initial model based on sequence similarity was refined based on predicted secondary structure. The ECD and TM regions were modeled individually, combined in one PDB file, and then the chain break was fixed using Swiss PDB Viewer. Each subunit of the channel was modeled separately then combined to create a single PDB file containing coordinates for the complete trimer. Protonation states for the channel were set to mimic pH 7 based on the p$K_a$ values of Glu, Asp, and His residues calculated previously for ASIC1a (Liechti et al., 2010); Glu and Asp residues with a p$K_a$ > 7 were protonated in the model, whereas all His residues were deprotonated. The model was energy-minimized in water using GROMACS 3.3.1. Water was then removed from the PDB file, and poor rotamers were adjusted in Swiss PDB Viewer. Model quality was monitored using MolProbity (Davis et al., 2007).

**Modeling the π-TRTX-Pc1a–ASIC1a Complex.** HADDOCK v2.1 (Dominguez et al., 2003) was used for docking studies because it allows incorporation of experimentally derived information about residue flexibility and interaction surfaces. Residues Trp24, Arg26 and Arg27 of π-TRTX-Pc1a were defined as "active" ambiguous interactions restraints (AIRs) based on mutagenesis experiments described here. Toxin residues 24 to 29 were allowed to be flexible during docking based on the solution dynamics observed in NMR relaxation/dispersion experiments and MD simulations. In addition, unambiguous distance restraints were included for the disulfide bridges and hydrogen bonds in the toxin. All 25 models from the ensemble of π-TRTX-Pc1a structures were used for cross-docking against rASIC1a. Before docking, the protonation states of π-TRTX-Pc1a residues were set to mimic pH 7, with all Asp, Glu, and His residues deprotonated, because this is the optimal pH for binding of π-TRTX-Pc1a to ASIC1a (Salinas et al., 2006). HADDOCK was used to generate 2000 structures from rigid body docking, then semiflexible refinement and water refinement was performed to obtain the top 200 structures.

## Results

**Production of Recombinant π-TRTX-Pc1a.** Recombinant π-TRTX-Pc1a was produced previously using a *Drosophila melanogaster* expression system (Escoubas et al., 2003), but we explored the possibility of using *E. coli* as a more cost- and time-effective method. Venom toxins generally pose a challenge for recombinant expression because of the presence of multiple disulfide bonds, which cannot be formed within the cytoplasm of most cells as a result of the reducing environment (Tedford et al., 2001). To obviate this problem, we used an IPTG-inducible construct (Fig. 1A) that allowed an MBP-toxin fusion protein to be exported to the *E. coli* periplasm, where the cell's disulfide-bond processing machinery is located (Tedford et al., 2001). A TEV protease cleavage site between the MBP and toxin coding regions allowed simple removal of the MBP tag.

Using this system, π-TRTX-Pc1a was the major cellular protein produced after IPTG induction (Fig. 1B), and the toxin could be purified to >98% homogeneity (as judged by SDS-polyacrylamide gel electrophoresis, HPLC, and MS) using a combination of nickel affinity chromatography and rpHPLC (Fig. 1C). This bacterial expression system produces ~6 mg of correctly folded π-TRTX-Pc1a per liter of culture, a significant improvement over the 0.5 mg/liter obtained using the previously published *D. melanogaster* expression system (Escoubas et al., 2003). The recombinant toxin blocked ASIC1a currents in *X. laevis* oocytes with an $IC_{50}$ of 0.42 ±

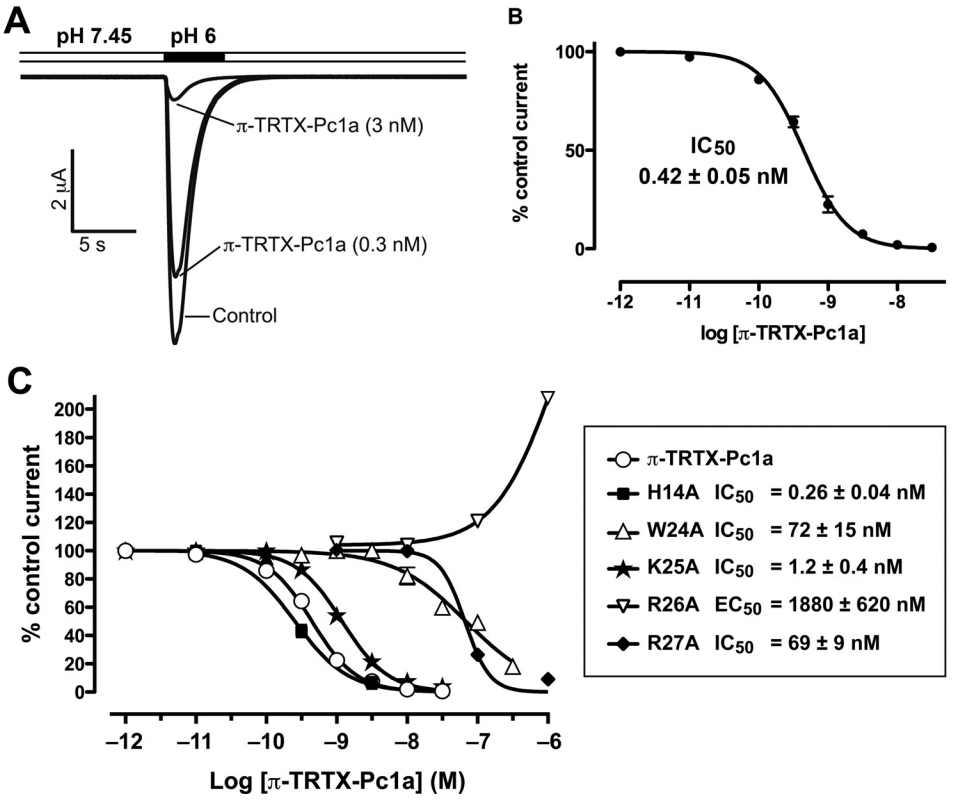


**Fig. 2.** Electrophysiological characterization of recombinant π-TRTX-Pc1a. A, current traces showing concentration-dependent inhibition of ASIC1a channels expressed in *X. laevis* oocytes by π-TRTX-Pc1a. ASIC1a currents were elicited by a pH drop from 7.45 to 6.0 (toxin applied for approximately 50 s between pH stimulations). B, logarithmic plot of the concentration-dependence of ASIC1a block by π-TRTX-Pc1a yielded an $IC_{50}$ value of 0.42 ± 0.05 nM. Each data point represents the mean ± S.E.M. of three to four independent experiments. C, logarithmic plot of the concentration-dependence of ASIC1a block by point mutants of π-TRTX-Pc1a. $IC_{50}$ values (mean ± S.E.M.) are given in the key.

0.05 nM (Fig. 2, A and B), which compares well with the previously published value of 0.9 nM (Escoubas et al., 2000). As reported previously for the native toxin, recombinant π-TRTX-Pc1a had no inhibitory effect on ASIC1b, ASIC2a, and ASIC3 currents in *X. laevis* oocytes at concentrations up to 30 nM (data not shown).

**Determination of a High-Resolution Solution Structure of π-TRTX-Pc1a.** The development of an efficient bacterial expression system allowed us to produce uniformly $^{13}C/^{15}N$-labeled π-TRTX-Pc1a for structure determination using heteronuclear NMR. $^{1}H_N$, $^{15}N$, $^{13}C_\alpha$, $^{13}C_\beta$, and $^{13}C'$ resonance assignments for the toxin were obtained from analysis of amide-proton strips in 3D HNCACB, CBCA(CO)NH, and HNCO spectra. Side-chain $^{1}H$ and $^{13}C$ chemical shifts were obtained primarily from 3D H(CC)(CO)NH-TOCSY and (H)CC(CO)NH-TOCSY spectra, respectively. However, some side-chain $^{1}H$ resonances that could not be unambiguously assigned from these spectra were assigned using a four-dimensional HCC(CO)NH-TOCSY experiment, which has the advantage of providing side-chain $^{1}H$-$^{13}C$ connectivities (Mobli et al., 2010). A fully assigned $^{1}H$-$^{15}N$ HSQC spectrum of π-TRTX-Pc1a is shown in Supplemental Fig. S1, and complete chemical shift assignments have been deposited in BioMagResBank (accession number 16468; http://www.bmrb.wisc.edu/).

Multiple hydrogen bonds involving backbone amide protons were identified from a long-range HNCO experiment, which has the advantage over hydrogen-deuterium exchange experiments of unambiguously identifying the hydrogen-bond acceptor. Figure 3 shows a selected region from the long-range HNCO spectrum in which several hydrogen bonds can be directly observed.

CYANA was used for automated NOESY assignment and

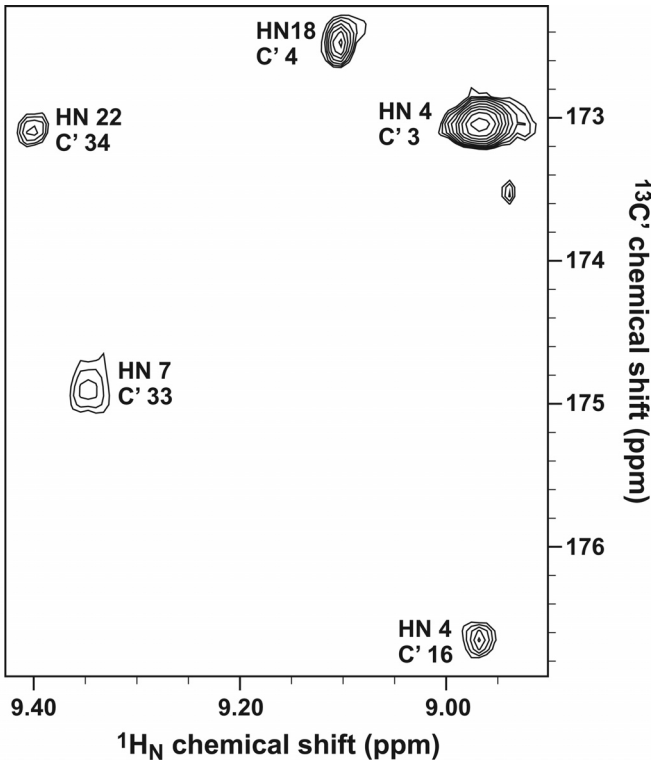


**Fig. 3.** Selected region from a long-range HNCO experiment. Hydrogen bonds are evident between the backbone amide protons of residues Ile4, Trp7, Cys18, and Glu22, and the backbone carbonyl oxygens of residues Asp16, Cys33, Ile4, and Val34, respectively. The peak in the upper right with a carbonyl carbon chemical shift of ~173 ppm is from the Cys3-Ile4 peptide bond (i.e., it is not indicative of a hydrogen bond).

TABLE 1

Statistical comparison of π-TRTX-Pc1a structures

All data are given as mean ± S.D. Only structurally relevant restraints, as defined by CYANA, are included. Root-mean-square deviation values were calculated over the well-defined regions of the structure (residues 2–36). Stereochemical quality according to MolProbity (http://molprobity.biochem.duke.edu). Clashscore is the number of steric overlaps >0.4 Å per $10^3$ atoms.

| | 2KNI | 1LMM |
|---|---|---|
| Experimental restraints | | |
| Interproton distance restraints | | |
| Intraresidue | 175 | 195 |
| Sequential | 152 | 111 |
| Medium range (i–j < 5) | 69 | 24 |
| Long range (i–j ≥ 5) | 151 | 44 |
| Hydrogen-bond restraints[a] | 20 | 12 |
| Disulfide-bond restraints | 9 | 9 |
| Dihedral-angle restraints (ϕ, ψ, $\chi_1$) | 69 | 21 |
| Total number of restraints per residue | 15.7 | 10.4 |
| Root-mean-square deviation to mean coordinate structure, Å | | |
| Backbone atoms | 0.25 ± 0.05 | 1.00 ± 0.21 |
| All heavy atoms | 0.87 ± 0.11 | 1.83 ± 0.24 |
| Stereochemical quality | | |
| Residues in most favored Ramachandran region, % | 83.9 ± 2.4 | 66.3 ± 4.6 |
| Ramachandran outliers, % | 0 ± 0 | 12.3 ± 4.1 |
| Unfavorable sidechain rotamers, % | 4.9 ± 1.8 | 34.7 ± 6.2 |
| Clashscore, all atoms | 0 ± 0 | 21.9 ± 7.8 |
| Overall MolProbity score | 1.69 ± 0.16 | 3.85 ± 0.15 |

[a] Two restraints were used per hydrogen bond.

structure calculation. Three hundred structures were calculated from random starting conformations, then the 25 conformers with highest stereochemical quality as judged by MolProbity (Davis et al., 2007) were selected to represent the solution structure of π-TRTX-Pc1a. Coordinates for the final ensemble of structures are available from the Protein Data Bank (code 2KNI).

Table 1 compares the precision and stereochemical quality of the π-TRTX-Pc1a structure determined in the current study with the previously published structure determined using only homonuclear NMR data (PDB code 1LMM). The average MolProbity score of 1.69 places the new ensemble of 25 structures in the 89th percentile relative to all other structures ranked by MolProbity, whereas the original ensemble ranks in the 4th percentile with an average MolProbity score of 3.85. The higher overall stereochemical quality of the new ensemble stems from a much lower clashscore (a measure of bad close contacts), higher Ramachandran plot quality, and more favorable side-chain rotamers (summarized in Table 1).

The new π-TRTX-Pc1a structure (Fig. 4A) is more precisely determined than the original ensemble [backbone root-mean-square deviation of 0.25 ± 0.05 Å over residues Asp2–Lys36 compared with 1.00 ± 0.21 Å for the previous ensemble (Escoubas et al., 2003)] because of the higher density of experimental restraints used in the structure calculations (summarized in Table 1). As demonstrated previously (Escoubas et al., 2003), the structure contains an inhibitor cystine knot motif (Pallaghy et al., 1994) in which the Cys17–Cys33 disulfide bond pierces a 14-residue ring formed by the other two disulfides and the intervening sections of the polypeptide backbone (Fig. 4C). Thus, π-TRTX-Pc1a comprises four intercystine loops (numbered 1–4 in Fig. 4A) bounded by N- and C-terminal "tails." The dominant secondary structure

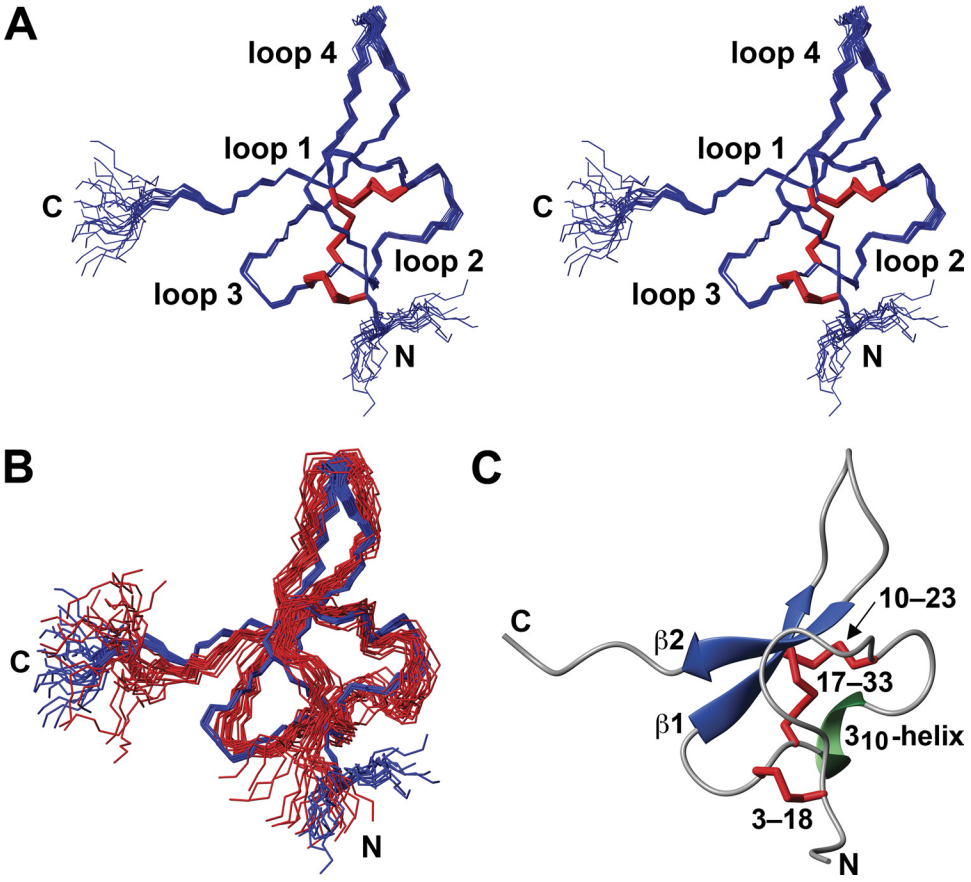


**Fig. 4.** A, stereo view of the ensemble of π-TRTX-Pc1a structures determined in this study. The peptide backbone is shown in blue and the three disulfide bonds are highlighted in red. The four intercystine loops and N and C termini are labeled. The structures are overlaid for optimal superposition over the backbone atoms of residues 2 to 36. B, overlay of the ensemble of π-TRTX-Pc1a structures determined in this study (PDB code 2KNI; blue) with the previously determined ensemble (PDB code 1LMM; red). The N and C termini are labeled. C, schematic of the π-TRTX-Pc1a structure determined in this study. The disulfide bonds (red), β-strands (blue), $3_{10}$-helix (green), and N and C termini are labeled.

feature is a β hairpin (residues 21–35) comprising β strands 1 (Leu21–Trp24) and 2 (Val32–Lys35) (Fig. 4).

Despite the significantly higher precision of the new ensemble, it is largely contained within the bundle of previously determined π-TRTX-Pc1a structures (Fig. 4B). It is noteworthy, however, that the higher precision of the new π-TRTX-Pc1a ensemble allows additional structural features to be recognized. Residues His14 to Asp16 within loop 2 form a single turn of $3_{10}$ helix that is not apparent in the original structure, in which this region is poorly defined, and residues Cys18 to Leu21 at the outer edge of loop 3 form a well defined β turn (Fig. 4, A and C). Loops 1 and 4 are also much better defined than in the original ensemble (see Fig. 4B).

**Definition of Pharmacophore Residues.** The marked electrostatic anisotropy of π-TRTX-Pc1a, in which a strong dipole moment emerges from the highly basic patch of Arg and Lys residues at the tip of loop 4 (residues 24 to 32), led to the suggestion that this hairpin loop is the functional surface of π-TRTX-Pc1a, the dipole moment being used to orient the toxin in the electric field of the ASIC1a channel (Escoubas et al., 2003). Subsequent docking studies have lent credence to this proposal (Pietra, 2009; Qadri et al., 2009). We decided to experimentally test this hypothesis by using the newly developed bacterial expression system to produce recombinant versions of π-TRTX-Pc1a in which residues in the β-hairpin loop were mutated to alanine. Specifically, we tested the ability of W24A, K25A, R26A, and R27A mutants to block ASIC1a (see Fig. 2C). The activity of a H14A mutant was also examined, because this residue lies adjacent to the β-hairpin loop and contributes to the electrostatic anisotropy of π-TRTX-Pc1a. Natural abundance $^{1}H$-$^{15}N$ HSQC spectra of the mutants were used to confirm that these point mutations did not perturb the toxin structure (data not shown).

Based on the initial structure determination, Lys25 was predicted to be involved in the interaction with ASIC1a (Escoubas et al., 2003), and this hypothesis seemed to be confirmed by two published models of the toxin-ASIC1a complex (Pietra, 2009; Qadri et al., 2009). We were surprised to find that the K25A mutant was almost equipotent with the wild-type toxin in blocking ASIC1a ($IC_{50}$ of 1.19 versus 0.44 nM for wild-type toxin) (Fig. 2C). Thus, we conclude that Lys25 is not essential for the interaction of π-TRTX-Pc1a with ASIC1a and probably makes few, if any, energetically favorable contacts with the channel. In contrast, mutation of both Trp24 and Arg27 to Ala caused a profound diminution in the ability of π-TRTX-Pc1a to block ASIC1a, both mutations resulting in an ~150-fold increase in the $IC_{50}$ (Fig. 2C). We conclude that both residues are critical for the interaction of π-TRTX-Pc1a with ASIC1a. Curiously, the R26A mutant was completely ineffective at blocking ASIC1a but, at high concentrations (>100 nM), it behaved as a positive modulator, increasing the size of the ASIC1a currents beyond control stimulations. We therefore conclude that Arg26 forms part of the π-TRTX-Pc1a pharmacophore. The H14A mutant was equipotent with wild-type toxin in blocking ASIC1a ($IC_{50}$ of 0.25 versus 0.44 nM for wild-type toxin; Fig. 2C), suggesting that the toxin pharmacophore is restricted to residues in the β-hairpin loop.

Because π-TRTX-Pc1a inhibits ASIC1a by shifting its steady-state desensitization to more alkaline pH, we investigated whether the mutations altered the functional effects of the toxin in addition to affecting its binding. All the mutants tested promoted an alkaline shift in steady-state desensitization similar to that caused by the wild-type peptide (see Table 2 and Supplemental Fig. 2). These results suggest that the observed changes in efficacy are probably due to a change in toxin binding affinity as opposed to an altered effect on channel gating. As expected, the R26A mutant did not cause a substantial alkaline shift in the SSD curve, but it did shift the pH-dependence of activation to more alkaline values.

TABLE 2

Mutant versions of π-TRTX-Pc1a promote a shift in the steady-state desensitization of rASIC1a to lower proton concentrations

Data are expressed as the mean ± S.E.M. calculated from measurements on four cells.

| π-TRTX-Pc1a | $pH_{50}$ | |
|---|---|---|
| | Steady-State Desensitization | Activation |
| Absence of toxin (control) | 7.33 ± 0.01 | 6.32 ± 0.01 |
| Wild-type toxin | 7.53 ± 0.02* | |
| π-TRTX-Pc1a | | |
| H14A | 7.46 ± 0.02* | |
| W24A | 7.54 ± 0.02* | |
| K25A | 7.55 ± 0.01* | |
| R26A | 7.42 ± 0.01*# | 6.72 ± 0.05* |
| R27A | 7.52 ± 0.01* | |

* $p < 0.01$ compared with control $pH_{50}$ (unpaired $t$ test).
# $p < 0.05$ compared with $pH_{50}$ in the presence of wild-type toxin (unpaired $t$ test).

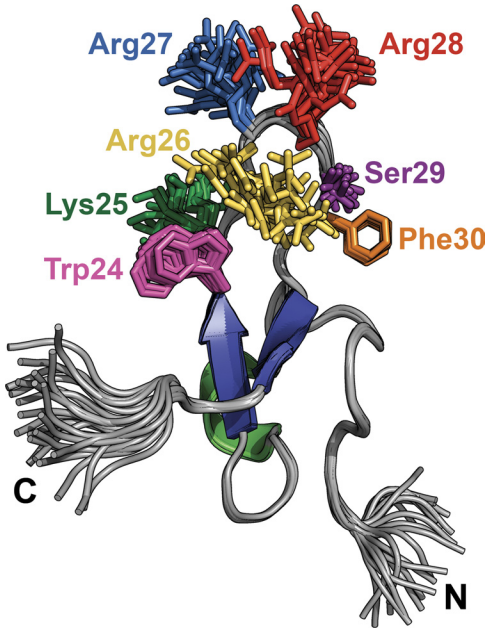


**Fig. 5.** Schematic of the ensemble of π-TRTX-Pc1a structures highlighting the side chains of residues in the functionally critical β-hairpin loop (loop 4). The β-strands and $3_{10}$-helix are shown in blue and green, respectively. The side chain of Glu31 has been omitted for the sake of clarity. Loop 4 side chains and the N and C termini are labeled.

**Structure and Dynamics of the Channel-Binding Loop.** Because the mutagenesis studies described above revealed that the pharmacophore of π-TRTX-Pc1a is most likely confined to the β-hairpin loop, we were particularly interested in the orientation of side chains within this loop, because they were poorly defined in the original ensemble of structures (Escoubas et al., 2003). Although markedly more precise than the previous structure, most side chains in this loop (with the exception of Phe30) are still poorly defined in

the new ensemble (Fig. 5). There are two likely explanations for the poor definition of these side chains compared with the remainder of the peptide: 1) a lower density of distance restraints, not because of intrinsic structural disorder, but due to ambiguous NOEs resulting from overlapping chemical shifts for protons in the side chains of Lys25, Arg26, Arg27, and Arg28 or 2) enhanced side-chain dynamics. A number of observations made during the process of compiling sequence-specific resonance assignments support the latter hypothesis. Resonances from residues within loop 4, in particular those of Lys25, were often broad or not present in various spectra, suggestive of interconversion between two or more conformations. For example, there was a complete absence of side-chain $^{13}C$-$^{1}H$ correlations for Lys25 in the $^{13}C$-edited NOESY-HSQC spectrum, and no correlations for the $C_\alpha$ of Lys25 and Glu31.

Given the critical importance of loop 4 for the interaction between π-TRTX-Pc1a and ASIC1a, we chose complementary experimental and computational approaches to probe the dynamics of this loop relative to other regions of the toxin. We first performed 5-ns MD simulations of the motion of π-TRTX-Pc1a in water. The order parameters ($S^2$) from the MD simulations were then calculated using windows of 100, 200, or 500 ps (windows significantly smaller than the estimated rotational correlation time of the peptide) and averaged over the course of 5 ns. All analyses showed consistent results regardless of time window used. Thus, for simplicity, results are only shown for analysis of the 100-ps windows (Fig. 6).

As expected from the new ensemble of structures, the N and C termini of the toxin have the lowest order parameters, and these regions are presumed to be extremely flexible in solution. There were only two other regions with $S^2 < 0.7$ [residues 15 to 16 in loop 2 and residues 25 to 30 in loop 4 (see Fig. 6)], a result that is consistent with the disorder associated with loop 4 side chains in the calculated ensemble of structures.

We next examined the backbone dynamics of π-TRTX-Pc1a using NMR spin relaxation and relaxation dispersion measurements and compared this with the dynamics predicted by MD simulations. The order parameter $S^2$, which is indicative of motions on the picosecond-to-nanosecond time scale, and the chemical/conformational exchange rate $R_{ex}$, which is indicative of motions on the low microsecond time scale, were determined from model-free analysis of the $^{15}N$ longitudinal relaxation rate ($R_1$), transverse relaxation rate ($R_2$), and steady state {$^{1}H$}-$^{15}N$ NOE data (see Supplemental Fig. S3). For most residues, the $S^2$ values calculated from the MD simulations and NMR relaxation data are in good agreement (see comparison in Fig. 6). The NMR data revealed picosecond-to-nanosecond scale motions for most residues in π-TRTX-Pc1a, with particularly low $S^2$ values for residues at the N and C termini as well as residue 14 in loop 2 and residues 26 to 27 in loop 4 (Fig. 7A, top; see also Supplemental Table S2). In addition, the spin relaxation experiments yielded significant $R_{ex}$ values for most residues in loop 4, indicative of motion on the low microsecond time scale (Fig. 7A, bottom).

To confirm the suspected motion in loop 4 over the μs-ms timescale, we performed $R_2$ relaxation dispersion experiments, which are better suited than spin relaxation experiments for examining motion on this timescale. Analysis of the relaxation dispersion data revealed significant motion on the microsecond-to-millisecond time scale in loop 2 (residues 8 and 12) and loop 4 (residues 25 and 30) (Fig. 7B; see also Supplemental Table S3). We therefore conclude, as summarized schematically in Fig. 7C, that before binding ASIC1a, the pharmacophore-containing loop 4 of π-TRTX-Pc1a undergoes significant motion over a wide range of time scales. This motion clearly limits the utility of rigid-body docking approaches for modeling the π-TRTX-Pc1a:ASIC1a complex.

**Modeling the π-TRTX-Pc1a:ASIC1a Interaction.** To perform restraints-based docking of π-TRTX-Pc1a and ASIC1a, we initially built a homology model of rat ASIC1a. Although models of human ASIC1a were used in previous docking studies (Pietra, 2009; Qadri et al., 2009), we chose instead to use rASIC1a, because the experimentally derived docking restraints were derived from two-electrode voltage-clamp experiments on this channel and because π-TRTX-Pc1a binds less avidly to human ASIC1a (data not shown). The ECD of rASIC1a was modeled from the 1.9-Å resolution structure of a nonfunctional cASIC1 construct in which most of the cytoplasmic regions of the channel had been removed (Jasti et al., 2007), leading to a nonphysiological orientation for the TM helices (Gonzales et al., 2009). Thus, the TM regions were instead modeled from a lower resolution struc-

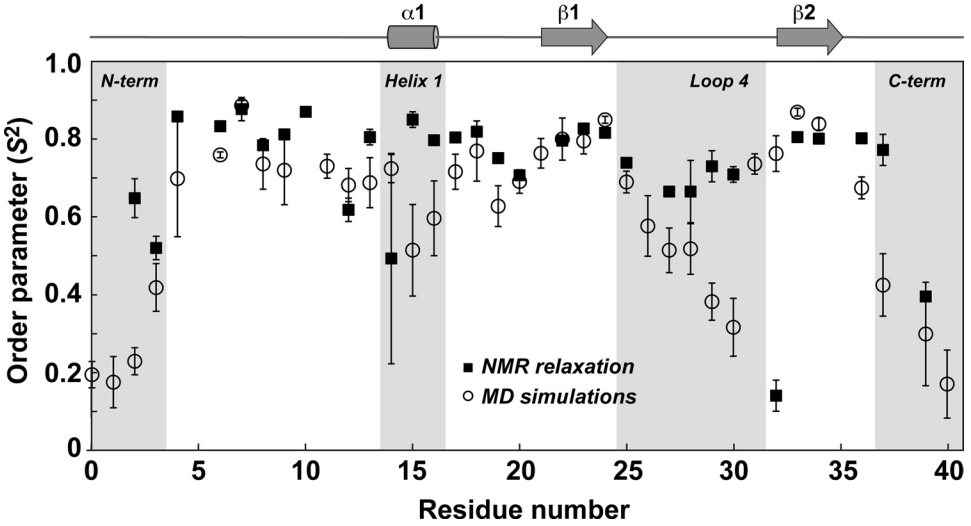


**Fig. 6.** Comparison of the average order parameters extracted from molecular dynamics simulations on π-TRTX-Pc1a using 100-ps windows (○) with the order parameters obtained from NMR relaxation experiments (■). Error bars indicate S.D. Residue '0' is the vestigial N-terminal serine residue resulting from TEV cleavage of the fusion protein. The secondary structure of the toxin is indicated at the top of the figure and the gray shading highlights regions of significant flexibility ($S^2 < 0.7$). "N-term" and "C-term" indicate the N- and C-terminal regions.

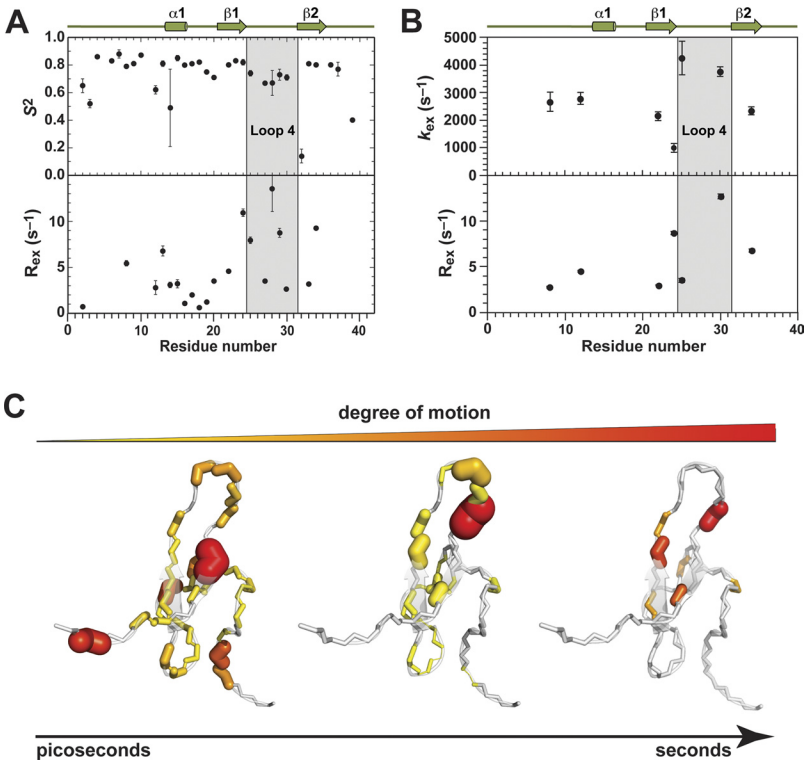


**Fig. 7.** A, model-free order parameter ($S^2$, top) and chemical/conformational exchange rate ($R_{ex}$, bottom) for $\pi$-TRTX-Pc1a extracted from NMR spin relaxation experiments. Low $S^2$ values for loop 4 (residues 25–31) indicate fast time scale motion in this region of the peptide. Large $R_{ex}$ values for this region also suggest motion on the low microsecond time scale. B, $k_{ex}$ (top) and conformational/chemical exchange rate constant ($R_{ex}$, bottom) for $\pi$-TRTX-Pc1a extracted from NMR relaxation dispersion experiments. Motion over the microsecond-to-millisecond time scale is predominantly present within loop 4. Extracted values fit best to fast exchange model, except residue 24, which is in slow exchange (minor population of 0.8%). C, structure of $\pi$-TRTX-Pc1a with degree of motion coded by color and width of the polypeptide chain. More motion is indicated by a color gradient from yellow to red and by increasing line thickness. The whole molecule is highly mobile on the picosecond-to-nansecond time scale as indicated by the color-coded $S^2$ values (left). Only residues within the loop 4 are mobile over the low microsecond time scale as indicated by the color-coded $R_{ex}$ values extracted from relaxation experiments (middle). Only a few residues, mostly within or adjacent to loop 4, were detected with motions on the microsecond-to-millisecond time scale as indicated by the color-coded $R_{ex}$ values from relaxation dispersion experiments (right).

ture of a functional cASIC1 construct in which inclusion of more cytoplasmic regions led to a different orientation of the TM helices that is considered more representative of the in vivo state of the channel based on comparisons with the corresponding region of the $P2X_4$ receptor (Gonzales et al., 2009). The structure of the ECD in the rASIC1a model was very similar to that in the high-resolution cASIC1 structure (root-mean-square deviation of 0.5–0.7 Å over 416–420 residues, depending on the chain), which is not surprising given the high level of sequence identity between the two channels (90%). The stereochemical quality of the rASIC1a model is comparable with that of the cASIC1 templates (see Supplemental Table S1).

Blind docking of our refined $\pi$-TRTX-Pc1a structure onto the homology model of rASIC1a confirmed that the toxin binds to the acidic pocket of the channel as shown previously (Pietra, 2009; Qadri et al., 2009). To refine the molecular details of this interaction, ambiguous interaction restraints derived from the mutagenesis studies were then used to drive the docking of $\pi$-TRTX-Pc1a onto the model of rASIC1a using HADDOCK. Residues Trp24, Arg26, and Arg27 of $\pi$-TRTX-Pc1a were defined as "active" AIRs on the basis of mutagenesis experiments. In addition, the backbone and side chains of toxin residues 24 to 29 were allowed to be flexible during the final stages of docking because of the significant molecular motion observed for these residues in NMR relaxation/dispersion experiments and MD simulations.

Very few studies have examined which residues on ASIC1a are required for interaction with $\pi$-TRTX-Pc1a. However, a point mutant of Asp349 near the center of the proton-binding pocket was previously shown to decrease inhibition of ASIC1a by $\pi$-TRTX-Pc1a (Salinas et al., 2006). This residue is adjacent to residues 167 to 185 on the neighboring subunit, which were shown to be critical for binding of $\pi$-TRTX-Pc1a (Chen et al., 2006). Thus, to define a set of active AIRs on the channel, a point in the center of the acidic pocket was chosen and all residues within a 10-Å radius of this site with more than 30% solvent accessibility in the rASIC1a model were defined as AIRs (see Supplemental Fig. S4). All active residues on the channel were allowed to be semiflexible during docking.

In all of the top 200 water-refined solutions, $\pi$-TRTX-Pc1a docked to the same region of the channel, with loop 4 at the "tip" of the triangular-shaped toxin sandwiched in the acidic pocket between adjacent subunits (Fig. 8A). Furthermore, the various poses differ only by rotations around the functional tip of the toxin relative to the lowest energy structure (Fig. 8B). Despite this rotation, the key functional residues in loop 4 (particularly Trp24–Arg28) localize to the same site on the channel and overlay remarkably well. Thus, for the sake of clarity, the following discussion will focus on the top 10 solutions from the lowest energy cluster (i.e., the cluster with the lowest HADDOCK scores) (Fig. 8C).

The mean buried interface area in the top 10 structures (2000 ± 40 Å) was slightly higher than the average buried surface area of 1600 ± 400 Å for all protein-protein complexes in the PDB (Dominguez et al., 2003). Table 3 summarizes the observed hydrogen bond and nonbonded interactions in the top 10 poses, and the key interactions are shown schematically in Fig. 9. The interaction between the toxin and the channel is dominated by ionic interactions and, as anticipated, each of the three residues in loop 4 that cause a major reduction in $\pi$-TRTX-Pc1a activity when mutated to Ala (i.e., Trp24, Arg26, and Arg27) make significant contributions. The positively charged guanidino group of Arg26 forms an ion pair with the carboxyl group of Asp237, whereas the side chain amide proton of Arg26 forms a hydrogen bond with the carboxyl group of Glu235 (Fig. 9B). The guanidino group of Arg27 makes ionic interactions with the carboxyl groups of both Glu242 on subunit A of the channel and

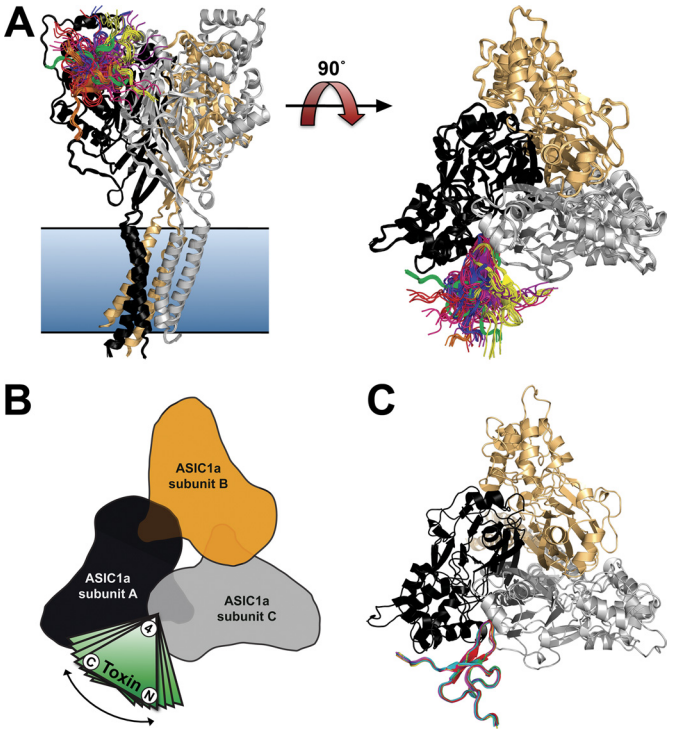


**Fig. 8.** A, representative poses from the top 200 water-refined solutions obtained from restraints-based docking of π-TRTX-Pc1a onto a homology model of rASIC1a. Some solutions have been omitted for the sake of clarity. Left, side-on view (i.e., parallel to the membrane surface); right, the same poses viewed from above the extracellular face of channel (i.e., orthogonal to the membrane). The transmembrane region is highlighted in blue, and the three subunits of the trimeric channel are shown in black, light orange, and gray. The toxin orientation relative to the channel can be grouped into seven clusters that are colored green (the lowest-energy cluster), red, blue, orange, magenta, pink, and yellow. B, schematic of the toxin-channel complex. In all of the top 200 poses, loop 4 of the triangular-shaped toxin (represented by ④) inserts into the acidic pocket of the channel and is sandwiched between neighboring subunits. The N and C termini of the toxin (indicated by the symbols) are directed toward the solvent, although the extended C-terminal segment makes sparse contacts with subunit A. The seven clusters differ only by a rotation around the axis indicated, with loop 4 firmly embedded in the acidic pocket in all cases. C, a view of the lowest-energy cluster viewed from the extracellular face of channel.

Asp407 on subunit C (Fig. 9C). The sidechain amide group of Trp24 forms a hydrogen bond with the side-chain carboxyl group of Asp349 (Fig. 9A). This latter interaction presumably explains why mutation of Asp349 decreases the ability of π-TRTX-Pc1a to inhibit ASIC1a (Salinas et al., 2006).

It was previously shown that π-TRTX-Pc1a modulation of human ASIC1a is completely abolished by a F352L mutation (Sherwood et al., 2009). However, even though the corresponding Phe350 residue in rASIC1a was included as an active restraint in the HADDOCK docking, we never observed an interaction between this channel residue and the toxin. The side chain of this residue points away from the acidic pocket in both the crystal structure of cASIC1 and the homology model of rASIC1a and is therefore not in a position to interact with the toxin. Moreover, the F352L mutation in human ASIC1a causes an acidic shift in the pH dependence of channel activation (Sherwood et al., 2009), suggesting that the channel conformation/gating mechanism is perturbed. Thus, we propose that mutation of Phe352 to Leu abrogates the binding of π-TRTX-Pc1a to human ASIC1a because it perturbs the conformation of the helix in which it resides, thus altering the spatial disposition of the adjacent Asp349 and Pro346 residues that are required for interaction with toxin residue Trp24.

Although the interactions between Trp24, Arg26, and Arg27 and residues on the channel are conserved in all low-energy clusters in the final docking solutions, the side chain of Lys25 has no consistent interaction with the channel. Although Lys25 interacts with channel residues Asp349 and Glu353 in the lowest-energy cluster, in most clusters it points away from the channel toward the solvent (see Supplemental Fig. S5). This is consistent with our data showing that mutation of Lys25 to Ala does not reduce the ability of π-TRTX-Pc1a to inhibit ASIC1a.

It is noteworthy that Trp24, Arg26, and Arg27 mostly interact with the same subunit of the channel (defined as subunit A in the current model). In contrast, although Arg28 was not included as an active AIR, the side chain of this toxin residue forms an ion pair with the carboxylate group of Glu219 on the adjacent subunit of the channel (subunit C in

TABLE 3

Hydrogen bonds and nonbonded contacts that occur between π-TRTX-Pc1a and rASIC1a in at least half of the poses in the lowest energy HADDOCK cluster

The number of solutions in the cluster in which the interaction is observed is given in parentheses.

| Toxin Residue | Hydrogen Bonds (<2.5 Å) | | Nonbonded Contacts (<3.9 Å) | |
|---|---|---|---|---|
| | Chain A | Chain C | Chain A | Chain C |
| Val11 | | | | ALA178 (8/10) |
| Trp24 | ASP349 (5/10) | | PRO346 (7/10) | |
| Lys25 | ASP349 (10/10)<br>GLU353 (10/10)<br>ASP237 (6/10) | | GLU353 (7/10) | GLY176 (9/10) |
| Arg26 | ASP237 (9/10)<br>GLU235 (9/10)<br>THR239 (6/10) | | THR236 (9/10) ASP237 (6/10) | |
| Arg27 | GLU242 (9/10)<br>ASP237 (6/10) | ASP407 (5/10) | | HIS173 (7/10) |
| Arg28 | | GLU219 (10/10)<br>GLN270 (6/10) | PHE241 (10/10)<br>GLU235 (6/10) | HIS173 (9/10)<br>MET221 (6/10) |
| Ser29 | GLU235 (10/10) | LYS391 (10/10) HIS173 (7/10) | | |
| Glu31 | LYS354 (10/10) | | | |
| Lys36 | GLU342 (7/10) | | | |
| Thr37 | GLU342 (10/10) | | | |
| Lys39 | GLU338 (10/10) GLU342 (10/10) | | GLU338 (5/10) | |
| Thr40 | GLU338 (10/10) | | | |

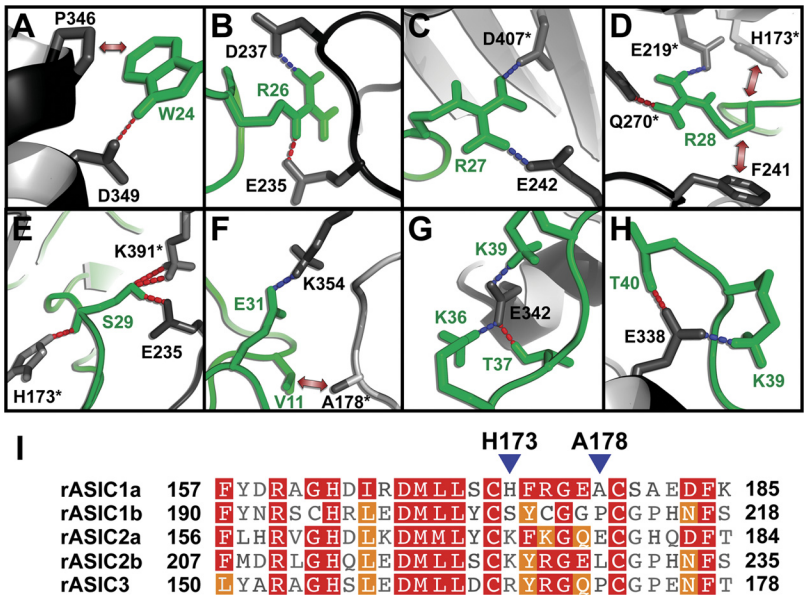


**Fig. 9.** Summary of key intermolecular interactions in the lowest-energy structure obtained from HADDOCK docking. The dominant interactions are shown for toxin residues Trp24 (A), Arg26 (B), Arg27 (C), Arg28 (D), Ser29 (E), Val11 and Glu31 (F), and Lys36, Thr37, Lys39, and Thr40 (G and H). Toxin and channel residues are shown in green and gray, respectively. Ion pairs are indicated by blue dashed lines, hydrogen bonds are represented as red dashed lines, and hydrophobic interactions are indicated by double-headed red arrows. Channel residues are from subunit A except those highlighted with an asterisk, which are from the adjacent subunit C. Note that most toxin residues make multiple interactions with rASIC1a; for example, as shown in C, Arg27 makes ionic interactions with both Glu242 on subunit A and Asp407 on subunit C. I, sequence alignment of domain 3 of rat ASIC1a (as defined in Salinas et al., 2006) with other ASIC subtypes. Residues that are identical or conservatively substituted (relative to ASIC1a) in at least four of the five subtypes are highlighted. Identical and conservatively substituted residues are highlighted in red and orange, respectively. Note that ASIC1a residues His173 and Ala178, which make key interactions with $\pi$-TRTX-Pc1a in the HADDOCK model, are not conserved in the other ASIC subtypes.

the current model) (Fig. 9D), implicating Arg28 as part of the toxin pharmacophore. We consequently predict that mutagenesis of Arg28 to virtually any other residue, with the possible exception of His and Lys, will impair toxin binding and activity. Other loop 4 residues that were identified from the docking as likely to be important for the interaction include Ser29 and Glu31 (Table 3; Fig. 9, E and F). C-terminal residues Lys36, Thr37, Lys39, and Thr40 also make favorable contacts with the channel (summarized in Table 3 and Fig. 9, G and H).

Numerous residues from the adjacent subunit C interact with the toxin (see Table 3). Most of these residues are conserved across all ASIC subtypes, His173 and Ala178 being the notable exceptions (Fig. 9I). His173 seems to play a major role in $\pi$-TRTX-Pc1a binding in that it interacts with three toxin residues (Arg27, Arg28, and Ser29; see Table 3) and makes more intermolecular contacts than any other residue in subunit C. Because His173 and Ala178 are present only in ASIC1a, we propose that they play a key role in determining the ability of $\pi$-TRTX-Pc1a to specifically block homomeric ASIC1a channels but not other homomeric or heteromeric ASIC channels.

## Discussion

The tarantula toxin $\pi$-TRTX-Pc1a is the most potent and selective blocker of ASIC1a discovered to date. It has a unique mechanism of action, shifting the steady-state desensitization of ASIC1a to more alkaline pH and rendering the channel inactive at physiological proton concentrations (Chen et al., 2005). Because ASIC1a is now recognized as a novel and broad ranging therapeutic target, understanding the molecular basis of its interaction with $\pi$-TRTX-Pc1a should aid the rational development of potential analgesics and neuroprotective drugs that target this channel. The recent determination of the crystal structure of chicken ASIC1 (Jasti et al., 2007; Gonzales et al., 2009) has opened up the possibility of using molecular docking studies to gain insight into this interaction. These crystal structures were determined at low pH and probably represent the desensitized state of the channel. This is fortuitous, because $\pi$-TRTX-Pc1a is believed to bind with higher affinity to the desensitized state of ASIC1a than to either the closed or open state (Chen et al., 2006).

The interaction between $\pi$-TRTX-Pc1a and a model of hASIC1a based on the cASIC1 structure was investigated in two previous docking studies (Pietra, 2009; Qadri et al., 2009) in which no experimental restraints were used to guide the docking. The toxin was found to bind to the same site on hASIC1a (i.e., the acidic pocket) in both studies, but in different orientations. Consequently, no definitive molecular model is currently available to guide drug development studies. We reasoned that molecular docking based on experimental restraints should produce a more reliable model for rational design of ASIC1a blockers.

To this end, we developed an efficient bacterial system for production of recombinant $\pi$-TRTX-Pc1a that allowed us to 1) determine a higher quality structure of the toxin, 2) examine its solution dynamics, and 3) use a panel of point mutants to define key components of the toxin pharmacophore. Although the new structure of $\pi$-TRTX-Pc1a is very precise and of high stereochemical quality, it seemed to show disorder in the $\beta$-hairpin loop (loop 4) containing key pharmacophore residues. We used a combination of MD simulations, NMR spin relaxation experiments, and NMR relaxation dispersion measurements to show that there is significant motion in the pharmacophore loop over a wide range of time scales (picoseconds to microseconds; see Figs. 6 and 7), supporting the apparent lack of precision for loop 4 residues in the NMR-derived toxin structure. Although the side chains of these residues are likely to be more rigid when the toxin binds to ASIC1a, it is critical that their intrinsic flexibility is taken into account in docking studies to prevent the formation of a structurally nonphysiological complex. Although a structure of $\pi$-TRTX-Pc1a bound to ASIC1a would be undoubtedly beneficial for rational structure-based design of mimetics that mimic the action of the toxin, understanding the conformational states that the peptide can access may also aid the design of mimetics.

**Defining the $\pi$-TRTX-Pc1a Pharmacophore.** We used a panel of point mutants to demonstrate that Trp24, Arg26,

and Arg27 in loop 4 are critical for the ability of π-TRTX-Pc1a to inhibit ASIC1a. It was initially surprising that mutation of Lys25, which is located in the middle of this positively charged loop, had no effect on the ability of the toxin to inhibit ASIC1a. However, close inspection of the new toxin structure reveals that the side chain of Lys25 lies on the face of the β-hairpin loop opposite that of the side chains of Trp24, Arg26, and Arg27 (Fig. 5). Moreover, in many of the final docking poses obtained for the π-TRTX-Pc1a–ASIC1a complex, this residue points away from the channel, thus providing an explanation for its lack of involvement in toxin activity.

**Modeling the π-TRTX-Pc1a–ASIC1a Interaction.** There were several key differences between the ASIC1a model used in the current study and those used in previous docking studies (Pietra, 2009; Qadri et al., 2009). First, we used rat rather than human ASIC1a, because π-TRTX-Pc1a binds more avidly to the rat channel (data not shown), and the majority of structure-activity relationship studies examining the interaction between π-TRTX-Pc1a and ASIC1a, including those reported here, used the rat channel. Second, we incorporated explicit flexibility for interacting residues at the toxin-channel interface based on our experimental data showing that the toxin pharmacophore is dynamic. Third, we were able to incorporate physiologically relevant protonation states for key ionizable residues in our model. Pietra (2009) used REDUCE (http://kinemage.biochem.duke.edu/software/reduce.php) for automatic protonation of His and Asp residues, whereas Qadri et al. (2009) did not describe the protonation states used in their model. The p$K_a$ of His, Asp, and Glu residues in ASIC1a were recently determined using a Poisson-Boltzmann continuum approach and homology models of hASIC1a (Liechti et al., 2010), and we used these values to yield the appropriate protonation states for these residues at pH 7.

We used HADDOCK for docking because it enabled the incorporation of ambiguous interaction restraints derived from mutagenesis data and movement of pharmacophore residues at the interaction interface during the simulated annealing process. The latter feature was considered critical because the intrinsic flexibility of the toxin pharmacophore that was revealed in the current study precludes the use of rigid body docking. Consistent with previous docking studies (Pietra, 2009; Qadri et al., 2009), π-TRTX-Pc1a was found to bind to the acidic pocket of ASIC1a (i.e., one of the sites responsible for activation of the channel by protons at acidic pH). Previous mutagenesis studies led to the conclusion that domains 3 and 5 of ASIC1a (i.e., residues 157–185 and 272–369, respectively) are intimately involved in binding π-TRTX-Pc1a (Salinas et al., 2006), and the majority of channel residues at the interaction interface in our docking model fall within these two domains.

In addition, residues from neighboring subunits were also involved in the interaction, and several of these residues (i.e., His173 and Ala178; see Fig. 9I) are present only in ASIC1a; this might explain, at least in part, why π-TRTX-Pc1a inhibits only homomeric ASIC1a channels. However, it is important to note that π-TRTX-Pc1a is believed to bind more tightly to the desensitized state of ASIC1a, whereas the potentiating effect of π-TRTX-Pc1a on ASIC1b is probably due to the toxin binding to the open (conducting) state of the channel. Because the open state of ASIC1 may have a substantially different conformation to the desensitized state, it is difficult to draw definitive conclusions from the current study about the interaction surface on ASIC1b that is recognized by π-TRTX-Pc1a.

Consistent with the results from our mutagenesis experiments, the toxin residues that make the largest number of interactions with the channel in the top 10 docking solutions (i.e., Trp24, Arg26, and Arg27) are those that have the largest impact on toxin function when mutated to Ala. In contrast, the side chain of Lys25 had no consistent interaction with the channel, in agreement with our data demonstrating that the K25A mutation does not reduce the ability of π-TRTX-Pc1a to inhibit ASIC1a.

A major contributor to the molecular events underlying the sensitivity of ASIC1a to acidic pH is the disruption of carboxyl-carboxylate pairs in the acidic pocket caused by the binding of protons (Jasti et al., 2007; Gründer and Chen, 2010). We found that π-TRTX-Pc1a docks into the acidic pocket of the channel and that arginine residues from the toxin mimic the action of protons by interacting directly with several of the anionic residues in these carboxyl-carboxylate pairs, including Asp237 and Asp349. Because of the subnanomolar affinity of π-TRTX-Pc1a for this site on the channel, we propose that the toxin effectively mimics the persistent activation by protons that leads to steady-state desensitization of ASIC1a when the extracellular pH is incrementally decreased (Sherwood and Askwith, 2009). This is consistent with the observation that π-TRTX-Pc1a shifts the steady-state desensitization of ASIC1a to higher pH and renders the channel inactive under normal physiological conditions (pH 7.3–7.4) (Chen et al., 2006).

In summary, our model of the ASIC1a–π-TRTX-Pc1a complex, which has been derived using a variety of complementary experimental approaches, is consistent with all currently available experimental data on the ASIC1a–π-TRTX-Pc1a interaction. This model greatly improves our understanding of the molecular details of this important interaction, and it should facilitate the development of novel therapeutics that mimic the action of π-TRTX-Pc1a.

#### Acknowledgments

Clones of rat ASIC1a, ASIC2a, and ASIC3 were a kind gift from Prof. John Wood (University College London) and rat ASIC1b was kindly provided by Prof. Stefan Gründer (University of Würzburg).

#### Authorship Contributions

*Participated in research design*: Saez, Chassagnon, Mark, Gooley, Rash, and King.

*Conducted experiments*: Saez, Mobli, Bieri, Chassagnon, Malde, Gamsjaeger, and Rash.

*Performed data analysis*: Saez, Mobli, Bieri, Chassagnon, Malde, Gamsjaeger, Mark, Gooley, Rash, and King.

*Wrote or contributed to the writing of the manuscript*: Saez, Mobli, Bieri, Chassagnon, Malde, Gamsjaeger, Mark, Gooley, Rash, and King.

#### References

Bieri M, d'Auvergne EJ, and Gooley PR (2011) relaxGUI: a new software for fast and simple NMR relaxation data analysis and calculation of ps-ns and μs motion of proteins. *J Biomol NMR* **50:**147–155.

Cabrita LD, Dai W, and Bottomley SP (2006) A family of *E. coli* expression vectors for laboratory scale and high throughput soluble protein production. *BMC Biotechnol* **6:**12.

Carnally SM, Dev HS, Stewart AP, Barrera NP, Van Bemmelen MX, Schild L, Henderson RM, and Edwardson JM (2008) Direct visualization of the trimeric

structure of the ASIC1a channel, using AFM imaging. *Biochem Biophys Res Commun* **372:**752–755.
Chen X, Kalbacher H, and Gründer S (2005) The tarantula toxin psalmotoxin 1 inhibits acid-sensing ion channel (ASIC) 1a by increasing its apparent $H^+$ affinity. *J Gen Physiol* **126:**71–79.
Chen X, Kalbacher H, and Gründer S (2006) Interaction of acid-sensing ion channel (ASIC) 1 with the tarantula toxin psalmotoxin 1 is state dependent. *J Gen Physiol* **127:**267–276.
Chen X, Qiu L, Li M, Dürrnagel S, Orser BA, Xiong ZG, and MacDonald JF (2010) Diarylamidines: high potency inhibitors of acid-sensing ion channels. *Neuropharmacology* **58:**1045–1053.
Cornilescu G, Delaglio F, and Bax A (1999) Protein backbone angle restraints from searching a database for chemical shift and sequence homology. *J Biomol NMR* **13:**289–302.
Davis IW, Leaver-Fay A, Chen VB, Block JN, Kapral GJ, Wang X, Murray LW, Arendall WB 3rd, Snoeyink J, Richardson JS, et al. (2007) MolProbity: all-atom contacts and structure validation for proteins and nucleic acids. *Nucleic Acids Res* **35:**W375–W383.
Dominguez C, Boelens R, and Bonvin AM (2003) HADDOCK: a protein-protein docking approach based on biochemical or biophysical information. *J Am Chem Soc* **125:**1731–1737.
Dubé GR, Elagoz A, and Mangat H (2009) Acid sensing ion channels and acid nociception. *Curr Pharm Des* **15:**1750–1766.
Escoubas P, Bernard C, Lambeau G, Lazdunski M, and Darbon H (2003) Recombinant production and solution structure of PcTx1, the specific peptide inhibitor of ASIC1a proton-gated cation channels. *Protein Sci* **12:**1332–1343.
Escoubas P, De Weille JR, Lecoq A, Diochot S, Waldmann R, Champigny G, Moinier D, Ménez A, and Lazdunski M (2000) Isolation of a tarantula toxin specific for a class of proton-gated $Na^+$ channels. *J Biol Chem* **275:**25116–25121.
Eswar N, Marti-Renom MA, Webb B, Madhusudhan MS, Eramian D, Shen MY, Pieper U, and Sali A (2006) Comparative protein structure modeling with MODELLER. *Curr Protoc Bioinformatics* **Chapter 5:**Unit 5.6.
Fletcher JI, Smith R, O'Donoghue SI, Nilges M, Connor M, Howden ME, Christie MJ, and King GF (1997) The structure of a novel insecticidal neurotoxin, ω-atracotoxin-HV1, from the venom of an Australian funnel web spider. *Nat Struct Biol* **4:**559–566.
Gonzales EB, Kawate T, and Gouaux E (2009) Pore architecture and ion sites in acid-sensing ion channels and P2X receptors. *Nature* **460:**599–604.
Gründer S and Chen X (2010) Structure, function, and pharmacology of acid-sensing ion channels (ASICs): focus on ASIC1a. *Int J Physiol Pathophysiol Pharmacol* **2:**73–94.
Güntert P (2004) Automated NMR structure calculation with CYANA. *Methods Mol Biol* **278:**353–378.
Hesselager M, Timmermann DB, and Ahring PK (2004) pH dependency and desensitization kinetics of heterologously expressed combinations of acid-sensing ion channel subunits. *J Biol Chem* **279:**11006–11015.
Jasti J, Furukawa H, Gonzales EB, and Gouaux E (2007) Structure of acid-sensing ion channel 1 at 1.9 Å resolution and low pH. *Nature* **449:**316–323.
Jensen JE, Durek T, Alewood PF, Adams DJ, King GF, and Rash LD (2009) Chemical synthesis and folding of APETx2, a potent and selective inhibitor of acid sensing ion channel 3. *Toxicon* **54:**56–61.
Kellenberger S and Schild L (2002) Epithelial sodium channel/degenerin family of ion channels: a variety of functions for a shared structure. *Physiol Rev* **82:**735–767.
King GF, Gentz MC, Escoubas P, and Nicholson GM (2008) A rational nomenclature for naming peptide toxins from spiders and other venomous animals. *Toxicon* **52:**264–276.
Krishtal OA and Pidoplichko VI (1981) A receptor for protons in the membrane of sensory neurons may participate in nociception. *Neuroscience* **6:**2599–2601.
Liechti LA, Bernèche S, Bargeton B, Iwaszkiewicz J, Roy S, Michielin O, and Kellenberger S (2010) A combined computational and functional approach identifies new residues involved in pH-dependent gating of ASIC1a. *J Biol Chem* **285:**16315–16329.
Mazzuca M, Heurteaux C, Alloui A, Diochot S, Baron A, Voilley N, Blondeau N, Escoubas P, Gélot A, Cupo A, et al. (2007) A tarantula peptide against pain via ASIC1a channels and opioid mechanisms. *Nat Neurosci* **10:**943–945.
Mobli M, Maciejewski MW, Gryk MR, and Hoch JC (2007) An automated tool for maximum entropy reconstruction of biomolecular NMR spectra. *Nat Methods* **4:**467–468.
Mobli M, Stern AS, Bermel W, King GF, and Hoch JC (2010) A non-uniformly sampled 4D HCC(CO)NH-TOCSY experiment processed using maximum entropy for rapid protein sidechain assignment. *J Magn Reson* **204:**160–164.
Oostenbrink C, Villa A, Mark AE, and van Gunsteren WF (2004) A biomolecular force field based on the free enthalpy of hydration and solvation: the GROMOS force-field parameter sets 53A5 and 53A6. *J Comput Chem* **25:**1656–1676.
Pallaghy PK, Nielsen KJ, Craik DJ, and Norton RS (1994) A common structural motif incorporating a cystine knot and a triple-stranded β-sheet in toxic and inhibitory polypeptides. *Protein Sci* **3:**1833–1839.
Pietra F (2009) Docking and MD simulations of the interaction of the tarantula peptide psalmotoxin-1 with ASIC1a channels using a homology model. *J Chem Inf Model* **49:**972–977.
Pignataro G, Simon RP, and Xiong ZG (2007) Prolonged activation of ASIC1a and the time window for neuroprotection in cerebral ischaemia. *Brain* **130:**151–158.
Qadri YJ, Berdiev BK, Song Y, Lippton HL, Fuller CM, and Benos DJ (2009) Psalmotoxin-1 docking to human acid-sensing ion channel-1. *J Biol Chem* **284:**17625–17633.
Salinas M, Rash LD, Baron A, Lambeau G, Escoubas P, and Lazdunski M (2006) The receptor site of the spider toxin PcTx1 on the proton-gated cation channel ASIC1a. *J Physiol* **570:**339–354.
Sherwood TW and Askwith CC (2009) Dynorphin opioid peptides enhance acid-sensing ion channel 1a activity and acidosis-induced neuronal death. *J Neurosci* **29:**14371–14380.
Sherwood T, Franke R, Conneely S, Joyner J, Arumugan P, and Askwith C (2009) Identification of protein domains that control proton and calcium sensitivity of ASIC1a. *J Biol Chem* **284:**27899–27907.
Sluka KA, Winter OC, and Wemmie JA (2009) Acid-sensing ion channels: a new target for pain and CNS diseases. *Curr Opin Drug Discov Devel* **12:**693–704.
Tedford HW, Fletcher JI, and King GF (2001) Functional significance of the β hairpin in the insecticidal neurotoxin ω-atracotoxin-Hv1a. *J Biol Chem* **276:**26568–26576.
Van Der Spoel D, Lindahl E, Hess B, Groenhof G, Mark AE, and Berendsen HJ (2005) GROMACS: fast, flexible, and free. *J Comput Chem* **26:**1701–1718.
Waldmann R, Champigny G, Bassilana F, Heurteaux C, and Lazdunski M (1997) A proton-gated cation channel involved in acid-sensing. *Nature* **386:**173–177.
Xiong ZG, Pignataro G, Li M, Chang SY, and Simon RP (2008) Acid-sensing ion channels (ASICs) as pharmacological targets for neurodegenerative diseases. *Curr Opin Pharmacol* **8:**25–32.

**Address correspondence to:** Prof. Glenn F. King, Institute for Molecular Bioscience, University of Queensland, 306 Carmody Road, St Lucia, QLD 4072, Australia; Phone: +61 7 3346–2025; Fax: +61 7 3346–2021; E-mail: glenn.king@imb.uq.edu.au